

QSO photometric redshifts using machine learning and neural networks

S. J. Curran^{*}, J. P. Moss and Y. C. Perrott

School of Chemical and Physical Sciences, Victoria University of Wellington, PO Box 600, Wellington 6140, New Zealand

Accepted —. Received —; in original form —

ABSTRACT

The scientific value of the next generation of large continuum surveys would be greatly increased if the redshifts of the newly detected sources could be rapidly and reliably estimated. Given the observational expense of obtaining spectroscopic redshifts for the large number of new detections expected, there has been substantial recent work on using machine learning techniques to obtain photometric redshifts. Here we compare the accuracy of the predicted photometric redshifts obtained from *Deep Learning* (DL) with the *k-Nearest Neighbour* (kNN) and the *Decision Tree Regression* (DTR) algorithms. We find using a combination of near-infrared, visible and ultraviolet magnitudes, trained upon a sample of SDSS QSOs, that the kNN and DL algorithms produce the best self-validation result with a standard deviation of $\sigma_{\Delta z} = 0.24$ ($\sigma_{\Delta z(\text{norm})} = 0.11$). Testing on various sub-samples, we find that the DL algorithm generally has lower values of $\sigma_{\Delta z}$, in addition to exhibiting a better performance in other measures. Our DL method, which uses an easy to implement off-the-shelf algorithm with no filtering nor removal of outliers, performs similarly to other, more complex, algorithms, resulting in an accuracy of $\Delta z < 0.1$ up to $z \sim 2.5$. Applying the DL algorithm trained on our 70 000 strong sample to other independent (radio-selected) datasets, we find $\sigma_{\Delta z} \leq 0.36$ ($\sigma_{\Delta z(\text{norm})} \leq 0.17$) over a wide range of radio flux densities. This indicates much potential in using this method to determine photometric redshifts of quasars detected with the Square Kilometre Array.

Key words: techniques: photometric – methods: statistical – galaxies: active – galaxies: photometry – infrared: galaxies – ultraviolet: galaxies

1 INTRODUCTION

Continuum surveys on the next generation of telescopes, e.g. the *Square Kilometre Array* (SKA), are expected to yield a large number of sources for which the redshifts are unknown. Even the *Evolutionary Map of the Universe* (EMU, Norris et al. 2011) on the *Australian Square Kilometre Array Pathfinder*, an SKA precursor, is expected to yield 70 million distant radio sources. Given the observational expense of high quality spectroscopic data, there is currently much activity in developing reliable photometry-based redshifts for distant sources (Lukens et al. 2019 and references therein).

The need for optical spectroscopy also causes a bias towards the most luminous sources, leaving the more obscured, gas-rich objects undetected (Curran et al. 2006; Curran et al. 2011). For these, the redshifts would ideally be obtained from the radio photometric properties, although this is proving difficult (Majic & Curran 2015; Norris et al. 2019), due to their relatively featureless spectral energy distributions (SEDs) and the limited number of radio sources for which redshifts are available (Morganti et al. 2015).

The optical band photometry methods generally use machine

learning models trained on the $u - g$, $g - r$, $r - i$ & $i - z$ colours of the *Sloan Digital Sky Survey* (SDSS), upon which they are self-validated (e.g. Richards et al. 2001; Ball et al. 2008). Due to the large redshift ranges being explored, Curran & Moss (2019) noted the importance of the bands beyond the visible and, including the WISE¹ and GALEX² colours as features in the *k-Nearest Neighbour* algorithm, Curran (2020) found a significant increase in the accuracy over using the SDSS colours alone, bringing the standard deviation in $\Delta z \equiv z_{\text{spec}} - z_{\text{phot}}$ down from $\sigma_{\Delta z[\text{data}]} = 0.525$ to 0.314.

The $FUV - NUV$, $NUV - u$, $u - g$, $g - r$, $r - i$, $i - z$, $z - W1$ & $W1 - W2$ colours of the SDSS sample also provided a suitable training set for another independent dataset of radio-loud sources (i.e. quasars, as well as the optically selected QSOs). In this paper, we use the full set of colours to compare other machine learning methods to the kNN, specifically *Decision Tree Regression* and *Deep Learning*, and again explore their transferability in training data for other, radio-selected, surveys, thus testing their poten-

^{*} Stephen.Curran@vuw.ac.nz

¹ *Wide-Field Infrared Survey Explorer* (Wright et al. 2010).

² *Galaxy Evolution Explorer* data release GR6/7 (Bianchi et al. 2017).

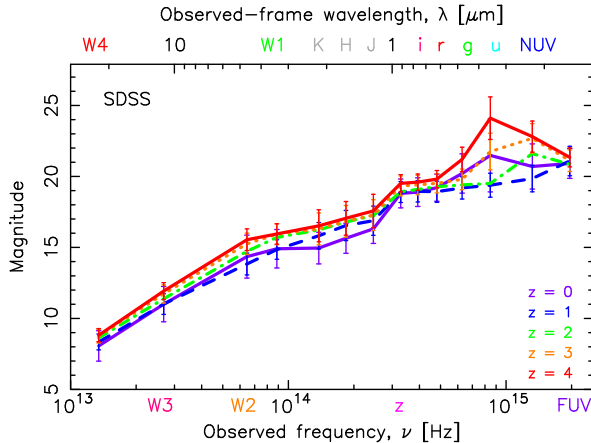


Figure 1. The mean magnitudes of the SDSS QSOs at redshifts of $z < 0.2$, $0.95 < z < 1.05$, $1.95 < z < 2.05$, $2.8 < z < 3.2$ and $3.5 < z < 4.5$. The positions of the mid-infrared to ultra-violet photometric bands are indicated along the top and bottom axes. The error bars show $\pm 1\sigma$ from the mean. The inversion of the trend at $\nu \gtrsim 10^{15}$ Hz, where the ultra-violet fluxes are expected to be generally undetectable, confirms our suspicion that there is confusion arising at the magnitude extremes.

tial in yielding reliable photometric redshifts for sources detected in forthcoming radio continuum surveys.

2 METHODS AND RESULTS

2.1 The training data

We extracted the first 100 000 QSOs with accurate spectroscopic redshifts ($\delta z/z < 0.01$) from the SDSS Data Release 12 (DR12, Alam et al. 2015). These were then matched to sources in the *NASA/IPAC Extragalactic Database* (NED), with the NED names being used to scrape the *Wide-Field Infrared Survey Explorer* (WISE), the *Two Micron All Sky Survey* (2MASS, Skrutskie et al. 2006) and GALEX databases. As per Curran (2020), in order to ensure a uniform magnitude measure between the SDSS and other samples (Sect. 3.2), for each QSO the PSF flux densities associated with the AB magnitudes which fell within $\Delta \log_{10} \nu = \pm 0.05$ of the central frequency of the band were added. Within each band range the fluxes were then averaged before being converted to a magnitude.³ This binning has the advantage of being applicable to other samples for which the SDSS photometry may not be directly available, but where there is other nearby photometry in other databases. That is, when using the SDSS to train other independent data sets (see Sect. 3.2).⁴ The mean magnitudes close to redshifts of $z = 0, 1, 2, 3$ and 4 of the sample are shown in Fig. 1. Retaining the sources detected in all nine bands (*FUV*, *NUV*, *u*, *g*, *r*, *i*, *z*, *W1*, *W2*) left a sample size 71 267 QSOs, which is 71% of the original data.

2.2 Algorithms

As previously (Curran 2020), we use the *FUV*–*NUV*, *NUV*–*u*, *u*–*g*, *g*–*r*, *r*–*i*, *i*–*z*, *z*–*W1* & *W1*–*W2* colours, in addition

³ For GALEX this was via $M = -2.5(\log_{10} S_\nu - 3.56)$, where S_ν is the specific flux density in Jy (<http://galex.stsci.edu/gr6/>).

⁴ In addition to yielding any radio photometry (see Sect. 3.2.5).

to the *r* magnitude, as features. As per typical practice, we train on 80% of the data and validate on the remaining 20%, quantifying the result via the standard deviation of the photometric redshifts from the spectroscopic. That is,

$$\sigma_{\Delta z} = \sqrt{\frac{1}{N} \sum_{i=1}^N \Delta z_i^2},$$

which we give for both the data and the Gaussian fit, since the latter is quoted in some of the literature (generally, $\sigma_{\Delta z}[\text{fit}] < \sigma_{\Delta z}[\text{data}]$). Also quoted is the *normalised standard deviation* (e.g. D’Isanto & Polsterer 2018; Luken et al. 2019), which is obtained from

$$\Delta z(\text{norm}) \equiv \frac{z_{\text{spec}} - z_{\text{phot}}}{z_{\text{spec}} + 1},$$

giving $\sigma_{\Delta z(\text{norm})} < \sigma_{\Delta z}$ for the same data. Finally, we also give the *median absolute deviation* (MAD),

$$\sigma_{\text{MAD}} \equiv 1.48 \times \text{median} |z_{\text{spec}} - z_{\text{phot}}|,$$

and the *normalised median absolute deviation* (NMAD),

$$\sigma_{\text{NMAD}} \equiv 1.48 \times \text{median} \left| \frac{z_{\text{spec}} - z_{\text{phot}}}{z_{\text{spec}} + 1} \right|,$$

e.g. Brescia et al. (2013) and Ananna et al. (2017), respectively. Note that, due to the randomisation of the training and validation data, the values of σ exhibit some slight variation about the values quoted.

2.2.1 *k*-Nearest Neighbour

The kNN algorithm, which compares the Euclidean distance between a datum and its k nearest neighbours in a feature space, has had some success in predicting photometric redshifts. However, the standard practice of using the $u - g$, $g - r$, $r - i$ and $i - z$ colours alone results in poor predictive power at $z \gtrsim 2$ and non-Gaussian distributions of Δz (Richards et al. 2001; Weinstein et al. 2004; Maddox et al. 2012; Han et al. 2016), with Curran (2020) obtaining $\sigma_{\Delta z}[\text{data}] = 0.525$. By including the GALEX colours as features in the `KNeighborsRegressor` function of `sklearn`⁵, this was reduced to $\sigma_{\Delta z}[\text{data}] = 0.352$, with the addition of near-infrared (NIR) *W1* & *W2* bands bringing this down to $\sigma_{\Delta z}[\text{data}] = 0.314$ (Curran 2020). Note that the addition of the mid-infrared (MIR) *W3* & *W4* bands did not have any noticeable benefit, while reducing the fraction of sources with detections in all of the bands from 79% to 57% of the SDSS sample.

The addition of the NIR bands tightened the $z_{\text{phot}} - z_{\text{spec}}$ correlation over all redshifts, probably due to these spanning $\lambda \sim 1 \mu\text{m}$ inflection in the SEDs (see Sect. 3.3.1), and inclusion of the UV bands had the most profound effect at low redshifts, probably due to sampling of the Lyman-break (see Sect. 3.3.3). Inclusion of other bands had been previously explored, giving similar results (e.g. Ball et al. 2008; Bovy et al. 2012; Brescia et al. 2013; Yang et al. 2017; Duncan et al. 2018; Salvato et al. 2019). Re-testing the kNN algorithm on our larger dataset, 71 267 cf. 26 301, we find significant improvement with $\sigma_{\Delta z}[\text{data}] = 0.236$ (Fig. 2, left), although, in addition to the larger sample, some of this will be due to the 80:20 training to validation ratio, cf. 50:50 (Curran 2020).

⁵ <https://scikit-learn.org/stable/>

2.2.2 Decision Tree Regression

Another common method used to determine photometric redshifts is the DTR algorithm, which builds a regression model in the form of a tree structure, branching a large dataset into smaller subsets starting from the entire dataset (the top node). This branches into two child nodes, based on a predefined decision boundary, with one node containing data above the decision boundary and one below (Ivezić et al. 2014). This decision-based bifurcation continues recursively until a predefined stopping criterion is reached. In this case, a certain value of Δz . Using the full set of colours as features for the `DecisionTreeRegressor` function of `sklearn`, we find a maximum tree depth of ≈ 10 to be optimal. Values greater than this result in over-fitting, making the Δz distribution less Gaussian with a wider spread in $\sigma_{\Delta z}[\text{data}]$ (although $\sigma_{\Delta z}[\text{fit}]$ narrows considerably). With $\sigma_{\Delta z}[\text{data}] = 0.333$ (Fig. 2, middle), the DTR algorithm does not appear to perform as well as the kNN.

2.2.3 Deep Learning

The concept of deep learning is to configure a computer architecture based upon the natural neurons found in biological brains, thus being very flexible, non-linear and sensitive to patterns in multi-dimensional data. The artificial neuron (“perceptron”) is the functional unit of the DL algorithm and consists of several layers: an input x_i ; weights and biases, w_i , defining the importance of the inputs; an activation function which transforms the weighted input – this is usually a non-linear function, such as the *hyperbolic tangent* (\tanh), a *sigmoid function*, or the more step-wise *Rectified Linear Unit* (ReLU) function. Each perceptron of the input layer may be connected to one, more or all of the other perceptrons in the adjacent layers, and the inputs are multiplied by the weights. The output then becomes

$$y_k = g \left(\sum_{j=0}^M w_{k,j}^{(N-1)} z_i^{(N-2)} \right),$$

where z_i is the output of the i th perceptron in the $N - 1$ level (Tagliaferri et al. 2003).

We use TensorFlow⁶, an off-the-shelf deep learning library. Since our output layer is an estimate of the redshift, the learning is supervised and, after testing various combinations of hyperparameters, we found a simple model with two *ReLU* layers and one *tanh* layer comprising 200 neurons each (giving 82 601 trainable parameters) to be the most effective, with larger and additional layers being of little benefit while considerably increasing the computation time. Since performing a regression, we employed the `keras RMSprop` optimizer, using early stopping with a patience of 10 to ensure against over-fitting.

As with the kNN and DTR methods, we use the standard 80:20 training-validation split, shuffling the data. Using the same colour combinations as the other algorithms, we find that the DL algorithm provides predictions of similar accuracy to the kNN method with $\sigma_{\Delta z}[\text{data}] = 0.236$ (Fig. 2, right). We note that the using the magnitudes as features in the DL algorithm, rather than the colours, gives a very similar result. Brescia et al. (2013); Pasquet-Itam & Pasquet (2018) and Beck et al. (2021) also use magnitudes as features for their algorithms and we interpret this as the neural net being free to decide how best to use this more elemental data.

⁶ <https://www.tensorflow.org>

2.3 Comparison of the algorithms

In Fig. 3, we show the performance of each of the algorithms for various sample sizes, using the same 80:20 training-validation split. From the standard deviation, we see that the DL algorithm generally performs best and, like the kNN, exhibits the expected anti-correlation between $\sigma_{\Delta z}$ and sample size. There is some scatter, most notably the DL point at $\sigma_{\Delta z} \approx 0.24$ & $n = 10\,000$, although this is to be expected due to the shuffling of the training and validation data in these single experiments. For the DTR algorithm, there is no apparent relationship between $\sigma_{\Delta z}$ and n , which also appears to be the case for all other measures. The superior performance of the DL method is confirmed by the other measures, where this generally has lower values of $\sigma_{\Delta z(\text{norm})}$, σ_{MAD} and σ_{NMAD} , while having higher values of the regression coefficient and a gradient which is generally closer to unity than the kNN and DTR algorithms.⁷

3 DISCUSSION

3.1 Comparison with previous deep learning results

Testing the three popular methods, we find deep learning to be the best in terms of self-validation. Comparing with other DL photometric redshift estimates of QSOs, Laurino et al. (2011) used the *Weak Gated Experts* method, which utilises a feature space (z_{phot}) which is partitioned by $FUV - NUV$, $NUV - u$, $u - g$, $g - r$, $r - i$, $i - z$ colour, and an *expert* maps each pattern of feature space to a target (z_{spec}), with the output of the experts defining a new feature space. This resulted in a sample of $\approx 27\,000$ from the original 105 783 QSOs of the SDSS DR7 (Schneider et al. 2010). Using a 60:40 training:validation split, the gate network uses a *softmax* activation function to map extracted patterns from the new feature space to the target space, which is an extension of the original feature space, with the added expert predictions. With this method they obtain $\sigma_{\Delta z}[\text{fit}] = 0.198$ and $\sigma_{\text{NMAD}} = 0.029$ compared to our 0.083 and 0.042, respectively.

Brescia et al. (2013) used the $u, g, r, i, z, NUV, FUV, W1, W2, W3, W4$, in addition to the UKIDSS DR9 Y, J, H, K near-infrared bands in a *Multilayer Perceptron Quasi-Newton Algorithm*, in which the Hessian of the error function finds the local minima and maxima of the activation function’s scalar error field. They use a 60:40 training:testing split, where 10-fold cross validation is performed on the training set. Using all of the SDSS, WISE, GALEX & UKIDSS bands, they obtain $\sigma_{\Delta z} = 0.15$ and $\sigma_{\text{MAD}} = 0.040$, outperforming our model (Fig. 2, right). However, this does require six additional bands, giving just 13% of the full sample, cf. 71% for ours. This would also lead to similar reductions in sample size when applied to other sources (see Sect. 3.2).

D’Isanto & Polsterer (2018) combined a *Mixture Density Network* and a *Deep Convolution Network* into a hybrid architecture, which they term a *Deep Convolutional Mixture Density Network*. Like us, they used a rectified linear unit applied to multiple layers, although they extracted the features from the SDSS DR7 & DR9 images. These comprise all five SDSS magnitudes and their colour combinations, although we find no extra benefit by combining both magnitudes and colours for the SDSS-W1-W2-GALEX data. The image-based algorithm automatically selects the best features,

⁷ These tend to be “dragged” down from unity by the excess of $z_{\text{spec}} \gg z_{\text{phot}}$ points at $z_{\text{spec}} \gtrsim 3$ (see Sect. 3.3.2).

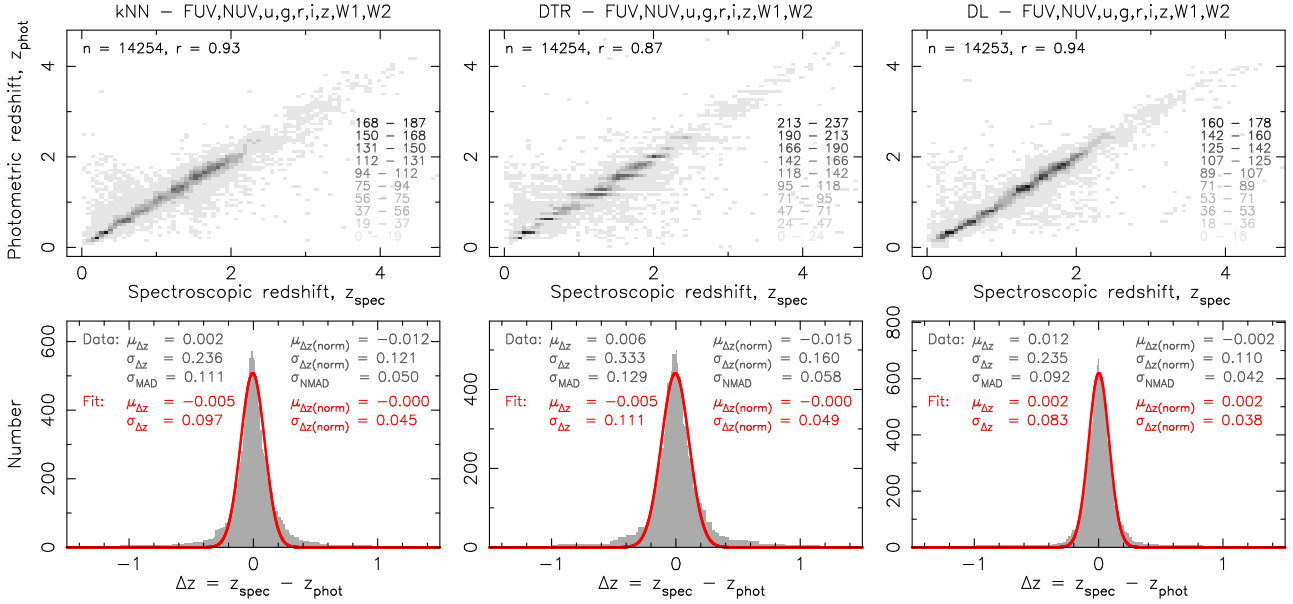


Figure 2. The predictions based on the colours and r magnitude from the different methods (kNN – left, DTR – middle, DL – right) using the SDSS sample, from a 80:20 training-validation split. In the scatter plot r shows the regression coefficient and the numbers to the right show the number of sources within each grey-scale pixel. The histogram shows the Δz distribution, where the mean and standard deviation are given for both the distribution and the Gaussian fit.

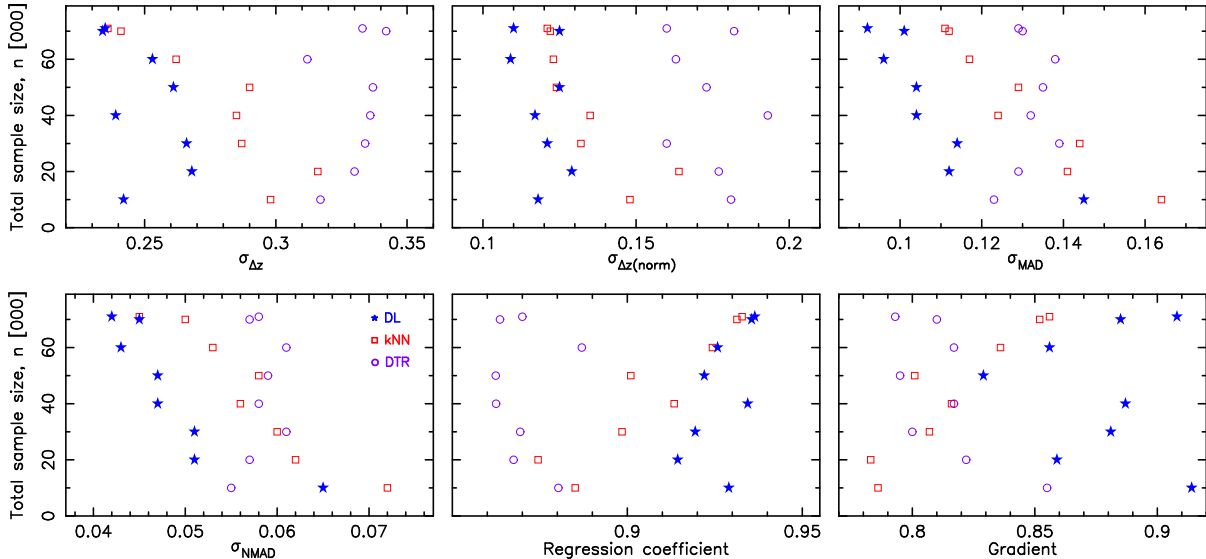


Figure 3. The total sample size versus the performance of each algorithm, as measured by the standard deviation, $\sigma_{\Delta z}$, the normalised standard deviation, $\sigma_{\Delta z(\text{norm})}$, the median absolute deviation, σ_{MAD} , the normalised median absolute deviation, σ_{NMAD} , the regression coefficient and the gradient of the linear regression between z_{phot} and z_{spec} . The kNN algorithm is represented by unfilled squares, the DTR by unfilled circles and the DL by filled stars. The DL algorithm has the best performance as judged by all indicators.

which required cluster computing to run. Using 185 000 sources from the SDSS DR7 and DR9 (Schneider et al. 2010; Pâris et al. 2012), from their 54:46 training:validation ratio, they obtained $\sigma_{\Delta z}[\text{fit}] = 0.217$, $\sigma_{\Delta z(\text{norm})}[\text{fit}] = 0.095$, and $\sigma_{\text{NMAD}} = 0.026$.

Pasquet-Itam & Pasquet (2018) used a *Convolutional Neural Network* (CNN) to detect and classify QSOs from the light curves in SDSS data (Stripe 82). Their architecture was based upon a three-layer CNN, which convolved the raw input with either a temporal convolution (time dependent magnitudes) or a filter convolution (integrated magnitudes). They used a hyperbolic tangent activation function applied to three layers and classified with an 80:20

training:validation ratio. Their architecture gives the probability of a signal being in a particular redshift range and, using the normalised root mean square, they found 80.4% of the photometric redshifts within $\Delta z(\text{norm}) < 0.1$, 87.1% within $\Delta z(\text{norm}) < 0.2$ and 91.8% within $\Delta z(\text{norm}) < 0.3$, compared to our 91.0%, 96.6% and 98.0%, respectively. Comparing their results with the kNN, support vector machine, a random forest classifier and a Gaussian process classifier, they found that their method compared most favourably to the kNN, especially for $z < 2.5$. The low number of quasars at higher redshifts means that their method was not trained well at $z \gtrsim 2.5$.

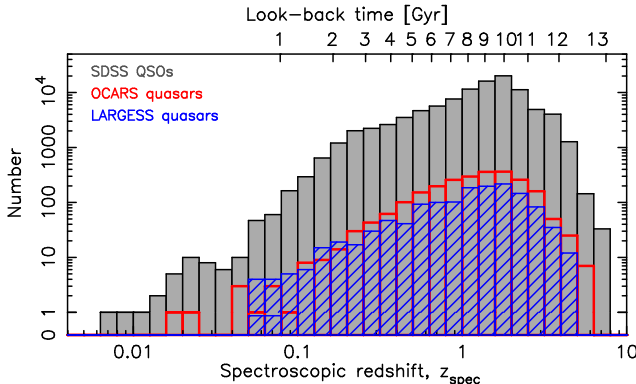


Figure 4. The redshift distribution for the SDSS (filled) and OCARS (unfilled) and LARGESS (hatched histogram) QSOs/quasars.

Similar to us, Beck et al. (2021) use TensorFlow with ReLu activation functions, but with all three-layers using 512 neurons and the *Adam* optimizer, upon the Pan-STARRS1 g, r, i, z, y magnitudes. Using an 80:20 training:validation split, they achieve a simulated $\Delta z(\text{norm})[\text{fit}] = 0.032$ and $\sigma_{\text{NMAD}} = 0.016$ over a limited $z_{\text{spec}} \approx 0 - 1$, acknowledging that this does not fully capture the variance in the data and includes galaxies. This redshift limitation permits reasonable predictions over such a small number of bands, due to minimisation of the shift in the rest-frame bands (Sect. 3.3.1), and is likely the reason for the more accurate predictions of galaxy, cf. QSO, redshifts (e.g. Ball et al. 2008; Laurino et al. 2011; Brescia et al. 2014; D’Isanto & Polsterer 2018; Ansari et al. 2019).

We summarise these in Table 1, where we see that our DL method produces similar results to the literature. However, unlike these other methods, which use magnitudes directly and validate on the same database, our scraping of the photometry allows us to apply the SDSS training to other (radio selected) samples, giving comparable results (Sect. 3.2).

3.2 Transferability to other surveys

Our goal is to obtain statistical redshift estimates for the radio continuum source surveys to be undertaken with the SKA and its pathfinders. Given this, we are interested in whether our methods are transferable to other (radio-selected) data, although, as outlined in Curran & Moss (2019), finding such datasets of sufficient size for which redshifts are available is a challenge. One dataset is the *Optical Characteristics of Astrometric Radio Sources* (OCARS) catalogue of *Very Long Baseline Interferometry* astrometry sources (Malkin 2018), a sample of flat spectrum radio sources with S -band (2–4 GHz) flux densities ranging from 15 mJy to 4.0 Jy (Ma et al. 2009).

Applying the kNN training of the full set of colours to the OCARS sources gave $\sigma_{\Delta z}[\text{data}] = 0.356$ for the 739 of the 3663 sources which had all of the required photometry (Curran 2020). Here, we perform the same test, but using the apparently superior DL model, in addition to testing this on the *Large Area Radio Galaxy Evolution Spectroscopic Survey* (LARGESS). Although both OCARS and LARGESS are independent, we see that the redshift distributions are well matched (Fig. 4).

We also test a sample from the *Faint Images of the Radio Sky at Twenty-Centimeters* (FIRST, Becker et al. 1995; White et al. 1997) survey, from which the redshifts have been obtained by matching with SDSS DR14 QSOs (Pâris et al. 2018). Although, ar-

guably not as independent a sample as OCARS or LARGESS, this provides 18 273 radio sources with redshifts with which to test the model.

3.2.1 OCARS

Applying the DL training to the OCARS data, we find $\sigma_{\Delta z}[\text{data}] = 0.362$ (Fig. 5, left), which is similar to the standard deviation obtained previously, using the kNN training. From the SEDs (Fig. 6), we see a similar pattern to the SDSS (Fig. 1), although the OCARS sources are generally brighter, across all magnitudes, especially at $z \sim 0$. We also note that the mean NIR band for the OCARS sources is relatively featureless.

3.2.2 LARGESS

LARGESS contains 10 856 optical redshifts for 12 329 radio sources (Ching et al. 2017) and comprises a mix of galaxies and quasars. Of the latter, there are 1608 for which the redshift reliability flag is $q \geq 3$ and 409 where $q = 5$.⁸ Of these, there are 1046 and 292 QSOs with all nine magnitudes, respectively. From Fig. 5 (middle), we see that the DL training on the SDSS sample provides an excellent prediction of the photometric redshifts, even for the $q < 5$ sources with $\sigma_{\Delta z}[\text{data}] = 0.297$. Limiting this to the $q = 5$ quasars only improves the prediction somewhat, giving $\sigma_{\Delta z}[\text{data}] = 0.217$, $\sigma_{\Delta z(\text{norm})}[\text{data}] = 0.107$, $\sigma_{\text{MAD}} = 0.102$ and $\sigma_{\text{NMAD}} = 0.052$. The SEDs bear more similarity to the SDSS QSOs than the OCARS quasars (Fig. 7). This could be due to the LARGESS sources having been matched with SDSS counterparts (Ching et al. 2017).

3.2.3 FIRST

The FIRST sample comprises 18 273 quasars common to the SDSS DR14. Although the full photometry is available (Pâris et al. 2018)⁹, we obtain the data as per the other samples, in order to ensure its compilation in a consistent manner. In particular, the GALEX data compiled in Pâris et al. have been force-photometered, recovering low signal-to-noise measurements not detected by GALEX. This, of course, leads to some matches not present in the GALEX GR6/7 catalogue and some extremely high magnitudes, reaching $NUV = 35.2$ and $FUV = 37.6$.¹⁰ From our matching, 6129 of the sample have all nine magnitudes, and, as may be expected, the quality of the photometric redshifts are close to those of the SDSS validation data (Fig. 2, right).

3.2.4 The 21-cm sample

Upon considering the scarcity of a large catalogue of radio sources with spectroscopic redshifts (cf. Drinkwater et al. 1997; Jackson et al. 2002; Brookes et al. 2008; Callingham et al. 2017), Curran & Moss (2019) tested their combination of magnitudes on the “21-cm sample”, a compilation of radio sources searched for

⁸ The redshift reliability flags range from $q = 0 - 5$ by increasing quality, where, for example, $q = 0$ – designates a “poor-quality (or missing) spectrum”, $q = 3$ – “a reasonably confident redshift” and $q = 5$ – an “extremely reliable redshift from a good-quality spectrum”.

⁹ https://www.sdss.org/dr14/algorithms/qso_catalog/

¹⁰ Of the 219 708 sources, 12 487 have $NUV > 25$ and 34 872 have $FUV > 25$, cf. Fig. 1.

Table 1. Comparison with other deep learning methods applied to QSOs. n gives the total number of sources (test + validation). Note that $\sigma_{\Delta z(\text{norm})}[\text{data}]$ is only quoted by Brescia et al. (2013) ($\sigma_{\Delta z(\text{norm})}[\text{data}] = 0.15$). The radio samples for this paper utilise the SDSS DR12 DL model (Sect. 3.2).

Reference	Sample	Photometry	z -range	n	Data		Fit	
					σ_{NMAD}	$\sigma_{\Delta z(\text{norm})}$	$\sigma_{\Delta z}$	$\sigma_{\Delta z(\text{norm})}$
Laurino et al. (2011)	SDSS DR7	FUV, NUV, u, g, r, i, z	$\lesssim 4$	27 000	0.029	—	0.198	—
Brescia et al. (2013)	SDSS DR7	15 bands	≤ 3.6	14 000	—	0.069	—	—
D’Isanto & Polsterer (2018)	SDSS DR9	u, g, r, i, z	$\lesssim 5$	185 000	0.026	—	0.217	0.095
Pasquet-Itam & Pasquet (2018)	SDSS DR7 (Stripe 82)	u, g, r, i, z	$\lesssim 2.6$	9000	—	0.349	—	—
Beck et al. (2021)	Pan-STARRS1	g, r, i, z, y	$\lesssim 1$	540 244	> 0.016	—	—	> 0.032
This paper	SDSS DR12	9 bands	≤ 4.9	71 267	0.042	0.110	0.083	0.038
	OCARS	...	≤ 4.8	649	0.063	0.170	0.107	0.050
	LARGELESS	...	≤ 4.7	1046	0.057	0.123	0.102	0.049
	FIRST	...	≤ 4.4	6129	0.048	0.110	0.089	0.042
	21-cm	...	≤ 3.6	28	0.124	0.140	0.165	0.093

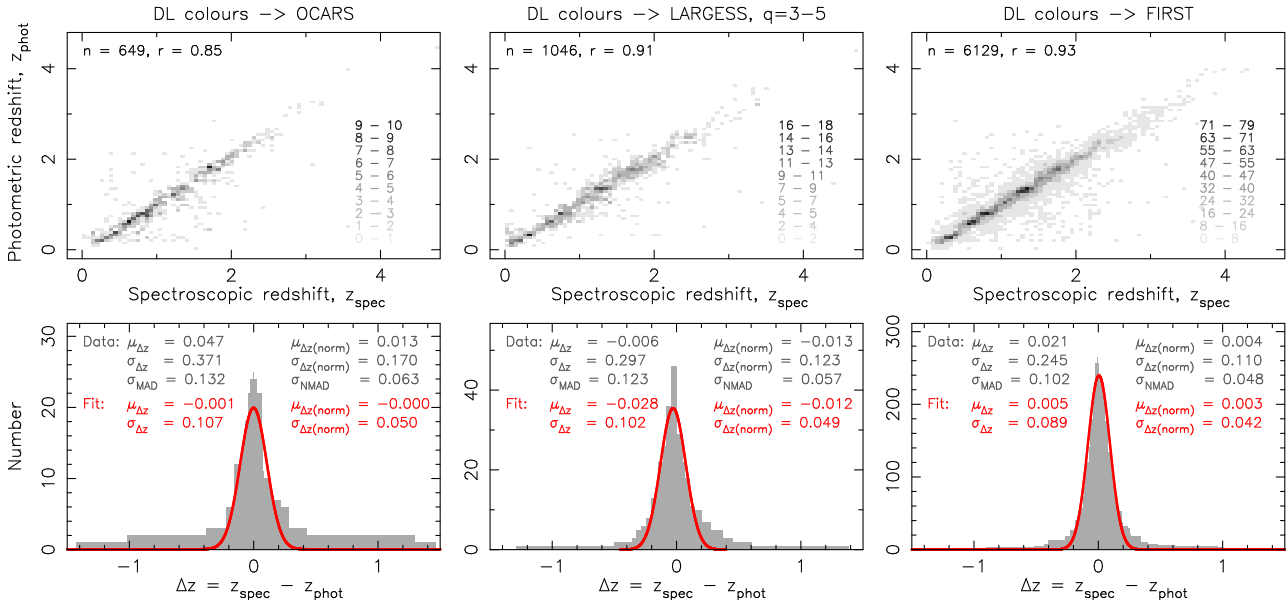


Figure 5. The predictions for the other samples trained using the colours from the DL training on SDSS data and validation on the OCARS data (left), the LARGESS $q = 3 - 5$ data (middle) and the FIRST data (right). Using the FUV, NUV, $u, g, r, i, z, W1, W2$ magnitudes directly gives similar results.

associated H I 21-cm absorption (Curran et al. 2019 and references therein). This comprises 819 radio-loud sources of known redshift, spanning $0.002 \leq z \leq 5.19$. Of this, only 262 are quasars of which only 28 have the full magnitude compliment. Nevertheless, we apply the DL training on the SDSS sample to predict the redshifts (Fig. 8) and see that the photometric redshifts are reasonable for this small sample.

3.2.5 Radio flux differences

Given the improved sensitivities, many of the sources detected by the SKA and its pathfinders are expected to have flux densities many times lower than the radio sources discussed here. For instance, EMU is expected to be sensitive to fluxes of $S_{\text{radio}} \lesssim 0.1$ mJy over large areas of the sky (Norris et al. 2011), whereas, being VLBI calibration sources, OCARS sources have fluxes $S_{\text{radio}} \gtrsim 0.1$ Jy. As mentioned above, the requirement of a catalogue of radio sources with spectroscopic redshifts limits the number of independent test samples. However, we should bear in mind that the training sample itself, although optically selected, contains

some radio sources. Of these, 3505 have at least one radio detection with the others either being unsearched or with fluxes below the sensitivity of current surveys.

Our mining of the source photometry (Sect. 2.1) also includes radio data and, in order to quantify the radio fluxes, we extract the $\nu < 10$ GHz values. Where there is more than one flux for a given source we average these. Showing the flux distributions in Fig. 9, we do see that the OCARS sources are much brighter than the SDSS, which in turn have a similar distribution to the LARGESS quasars, which are considered radio sources (Ching et al. 2017). We note that the OCARS distribution appears more symmetrical than those of the SDSS and LARGESS, which is suggestive of the weaker sources being truncated by the flux limited nature of the surveys. Due to small numbers, it is difficult to comment for the 21-cm quasars, although it is clear that the fluxes are about two orders of magnitude greater than the SDSS and LARGESS QSOs. Given the results of testing on both OCARS and LARGESS (Fig. 5), as well as the 21-cm sample (Fig. 8), we are confident that our algorithm can yield accurate photometric redshifts for sources with a wide range of radio flux densities.

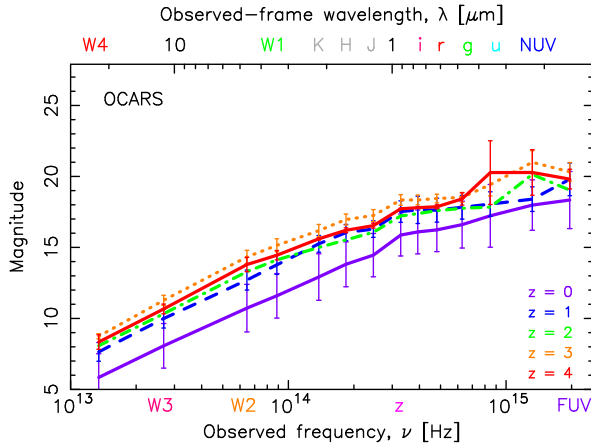


Figure 6. The mean magnitudes of the OCARS quasars at redshifts of $z < 0.2$, $0.95 < z < 1.05$, $1.95 < z < 2.05$, $2.8 < z < 3.2$ and $3.5 < z < 4.5$. The error bars show $\pm 1\sigma$ from the mean. Again, we see the same inversion for the high redshift FUV magnitudes, indicating their unreliability (cf. Fig. 1).

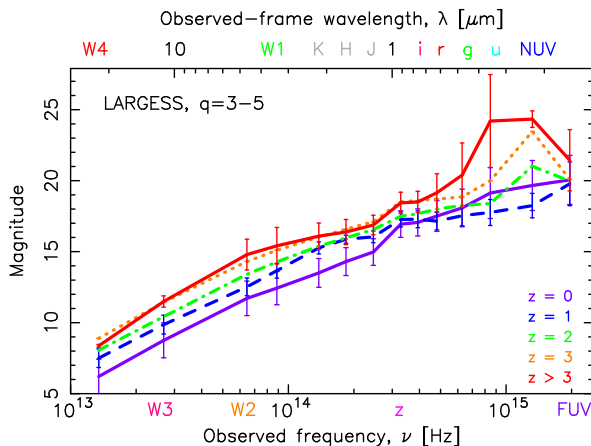


Figure 7. The mean magnitudes of the LARGESS $q = 3 - 5$ quasars at redshifts of $z < 0.2$, $0.95 < z < 1.05$, $1.95 < z < 2.05$, $2.8 < z < 3.2$ and $z > 3.2$ (due to a lower number of high redshift sources, Fig. 4). The error bars show $\pm 1\sigma$ from the mean. Again, we see the same inversion for the high redshift FUV magnitudes, indicating their unreliability (cf. Figs. 1 & 6).

3.2.6 Optical SEDs and radio loudness

In addition to the differences in radio flux, it is known that the mean optical and IR SEDs can differ between radio-loud and radio-quiet sources (Elvis et al. 1994). In Fig. 10, we show the mean SEDs from which we see that the LARGESS and SDSS are very similar, which is not surprising given their similarity in mean radio flux densities. As expected, the much more radio-loud OCARS and 21-cm quasars exhibit a substantial difference from the radio-quiet QSOs, particularly in the optical band. The SEDs do, however, overlap with the SDSS 1σ uncertainties, which is in line with the considerable variation between individual sources of the similar loudness noted by Elvis et al.. Also, the fact that the SDSS training applied to the other samples returns reasonable redshift predictions, suggests that the differences are small enough not to deviate significantly from the trained model, although they could contribute to the larger fraction of poor predictions for the OCARS data.

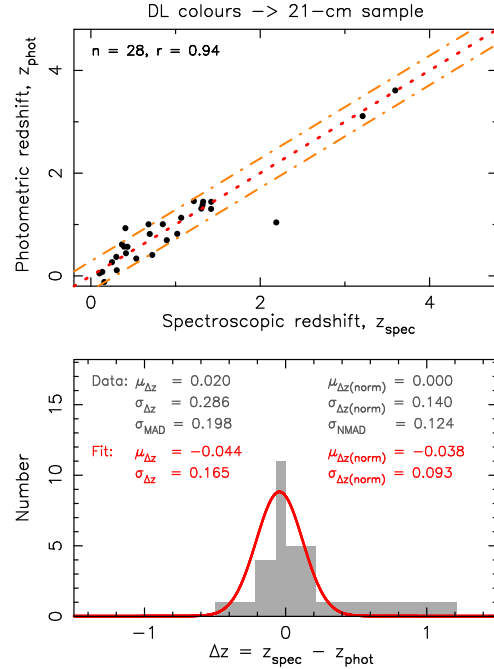


Figure 8. The photometric redshift prediction for the 21-cm sample. The dotted line shows $z_{\text{phot}} = z_{\text{spec}}$ and the broken lines $\pm \sigma_{\Delta z}[\text{data}]$.

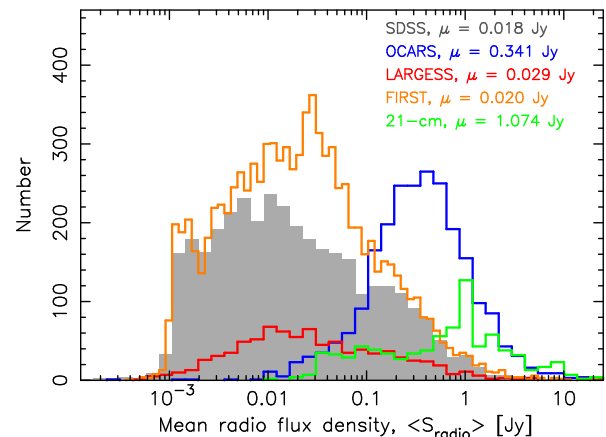


Figure 9. The mean radio flux densities of the QSOs/quasars in the SDSS, OCARS, LARGESS ($q = 3 - 5$), FIRST and 21-cm samples with measured ≤ 10 GHz flux densities. The legend shows the mean value of each distribution. For consistency, the fluxes for the FIRST sources are obtained in the same way as the other samples and the binning is twice as fine as for the other samples in order to fit within a similar range. The 1.4 GHz flux densities given in the FIRST catalogue range from 0.75 mJy to 14.8 Jy for this sample.

3.2.7 Matching coincidence

While the above does indicate that training the algorithm on the SDSS sources can provide reliable photometric redshifts for the radio-selected samples, the requirement of the $u, g, r, i, z, W1, W2, NUV, FUV$ magnitudes does mean that for a significant fraction of sources we cannot obtain a photometric redshift to the same reliability. Of the 1817 of the 3033 OCARS quasars which have at least one SDSS magnitude, 1136 have all five magnitudes, with 1034 of these also having $W1$ & $W2$, and 649 (21%) having all of the required photometry. For LARGESS, 1046

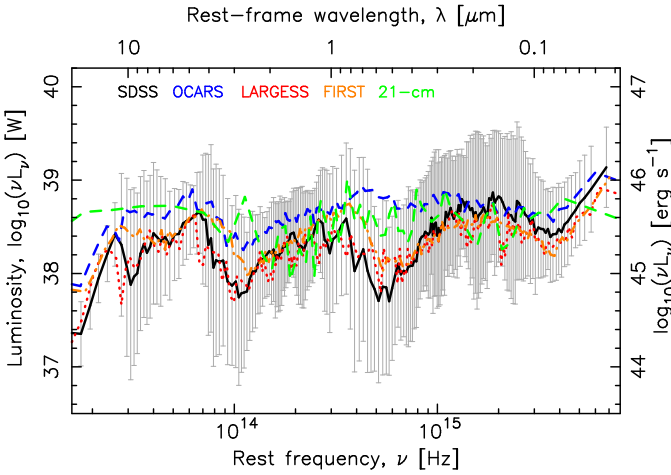


Figure 10. The mean SEDs of the various sub-samples. The error bars show the $\pm 1\sigma$ uncertainty in the binned SDSS luminosities.

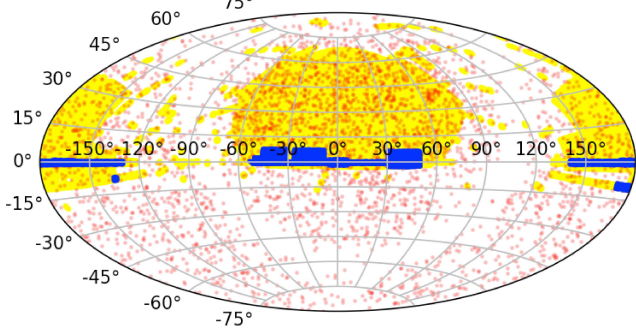


Figure 11. Right ascension and declination of the SDSS (northern sky – yellow), OCARS (all sky – red) and LARGESS ($-19^\circ < \delta < 8^\circ$ – blue) sources.

out of 1608 $q \geq 3$ quasars have the full magnitude complement, giving a matching coincidence of 65%. The limited OCARS–SDSS coordinate overlap (Fig. 11) highlights an important issue: Given that the SKA, and two of its pathfinders, will operate in the south, SkyMapper (Wolf et al. 2018) magnitudes should provide the optical magnitudes for the training of southern sources, upon the data becoming available.¹¹

3.3 Contribution of the IR and UV magnitudes

3.3.1 Physical interpretation

The improvement in the redshift prediction obtained by the inclusion of the infrared and ultra-violet photometry has previously been noted by Bovy et al. (2012) and Brescia et al. (2013). They attribute the inclusion of these to the breaking of the redshift degeneracy, which arises when using the u, g, r, i, z photometry alone (e.g. Richards et al. 2001; Maddox et al. 2012). From our own data, without the full photometry we see that the results degrade signifi-

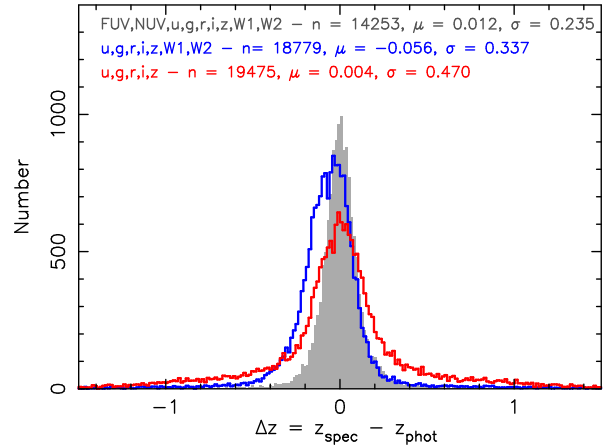


Figure 12. The Δz distributions using the SDSS colours only, the SDSS+WISE (W_1, W_2) and the full SDSS +WISE (W_1, W_2)+GALEX colour set..

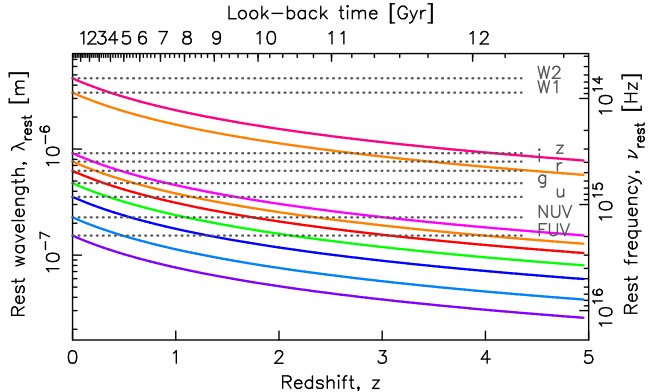


Figure 13. The dependence of source-frame wavelength with redshift for our photometric bands. The dotted lines on the left-hand ordinate show the observed-frame values and the curves branching off these the rest-frame wavelength as a function of source redshift.

cantly (Fig. 12), confirming the importance of the IR and UV data.

Curran & Moss (2019) found an empirical relationship between the redshift and the ratio of the $U - K$ and $W_2 - FUV$ colours in the *rest-frame* of the source. They hypothesised that this was due to the UV–NIR colours tracing the luminosity of the active galactic nucleus and, as seen from Fig. 13, the observed colours will depend strongly upon the redshift of the source. For instance, to measure the FUV and i luminosities at $z = 3$ requires the r and W_1 magnitudes in the observed-frame. As noted by Curran (2020), inclusion of the mid-infrared W_3 & W_4 magnitudes to the SDSS training has little effect on $\sigma_{\Delta z}$, which we confirm is also the case for the DL algorithm.¹²

Curran (2020) also noted the $\lambda \sim 1 \mu\text{m}$ inflection in the SED (e.g. Edelson & Malkan 1986; Barvainis 1987; Elvis et al. 1994), which was attributed to $\lambda \gtrsim 1 \mu\text{m}$ NIR emission from heated dust. An alternative explanation is that this is due to $\text{H}\alpha$ ($\lambda = 656 \text{ nm}$) emission, which, at $\lambda = 656 \text{ nm}$, would be apparent between the r and i bands at $z = 0$, shifting to W_1 at $z \gtrsim 4$. However, as per

¹¹ <http://skymapper.anu.edu.au>

¹² Their inclusion reduces the validation sample size from 14 253 to 11 045, but with no reduction in $\sigma_{\Delta z}$.

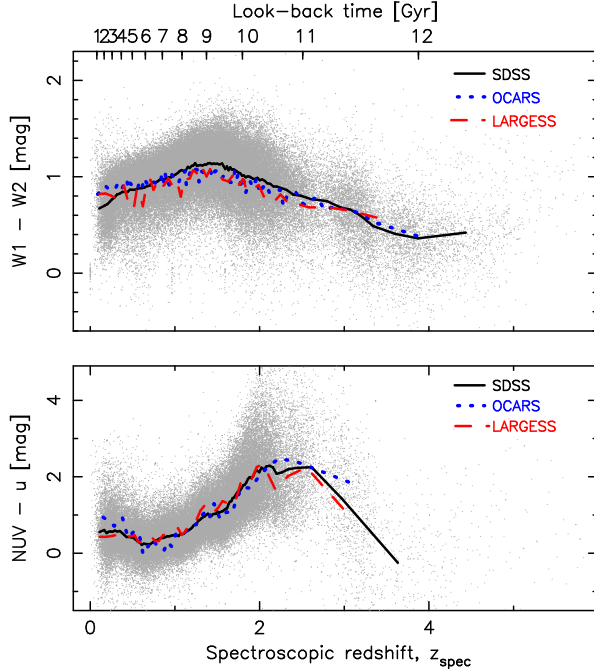


Figure 14. Top: The $W_1 - W_2$ colour versus redshift (cf. Assef et al. 2010; Reed et al. 2015). Bottom: The $NUV - u$ colour versus redshift. In both panels the points show the SDSS QSOs of the training sample and the traces show the average values of the three main samples.

Curran (2020), we see little evidence of the shifting of this feature in either of the SEDs (Figs. 1, 6 & 7), although there does appear to be inflections at $\approx 3 \mu\text{m}$ and $\approx 0.6 \mu\text{m}$ in the SDSS and related (LARGESS & FIRST) spectra (Fig. 10). A $\approx 3 \mu\text{m}$ feature has been previously noted in type-2 objects (Hickox et al. 2017) and so we attribute the $\approx 0.6 \mu\text{m}$ inflection to the rise of the “big blue bump”, due to thermal emission from the accretion disk.

Any inflection in Figs. 1, 6 & 7 could, of course, be somewhat masked by the limited J, H, K photometry of our sample (see Sect. 3.3.2), although the $W_1 - W_2$ colour does exhibit a clear redshift dependence for all samples (Fig. 14, top), where the peak at $z \sim 1.5$ corresponds to the rest-frame J, H, K bands. We also see that, despite our reservation of the applicability of the SDSS training to radio-loud sources (Sect. 3.2.5), both OCARS and LARGESS follow a similar evolution to the SDSS QSOs. This also applies at the other wavelength extreme, where the evolution of $NUV - u$ colour is also similar between the three main samples (Fig. 14, bottom)¹³, all exhibiting a steep evolution in $NUV - u$ at $z \gtrsim 1$ due to the Lyman-break.¹⁴

In the case of continuum emission from heated dust, we would expect an increase in redshift (and thus, luminosity) to cause an increase in the peak frequency of the modified black body emission (Curran & Duchesne 2018). This increase would counteract any redshift in the peak of the profile, curtailing any apparent shift in the NIR peak perhaps holding the observed NIR peaks at close to $\lambda \sim 1 \mu\text{m}$ in these relatively low resolution SEDs.

Lastly, the $W_1 - W_2$ colour is hypothesised to trace hot dust, from AGN activity, and the $W_2 - W_3$ colour warm dust, from star formation (Jarrett et al. 2011; Donoso et al. 2012). The

¹³ Given our suspicions about the FUV photometry, especially at high redshift (Figs. 1, 6 & 7), we choose this colour rather than $FUV - NUV$.

¹⁴ For the evolution of the constituent magnitudes see Fig. 19.

Table 2. Results of the 10-dimensional linear regression of the standardised ($\mu = 0, \sigma = 1$) magnitudes and z_{spec} versus Δz for the SDSS test data. m is the gradient, followed by the standard error. The intercept has a value of $c = 0.0371 \pm 0.002$. The final column gives the t -statistic.

Parameter	m	σ_m / \sqrt{n}	$t [\sigma]$
FUV	0.0222	0.002	9.115
NUV	-0.1490	0.003	-44.995
u	-0.0728	0.005	-15.964
g	0.1054	0.009	12.398
r	0.1693	0.011	16.093
i	0.1013	0.010	9.662
z	-0.1595	0.008	-19.877
W_1	-0.1643	0.007	-25.177
W_2	0.0040	0.007	0.608
z_{spec}	0.2236	0.003	80.920

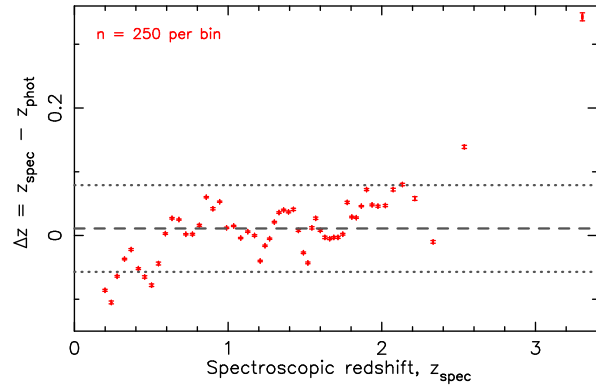


Figure 15. Δz versus z_{spec} for the SDSS test data binned into 50 bins of 250 QSOs each (leaving 3 remaining). The error bars show the standard error, σ/\sqrt{n} , and the dashed and dotted lines show the mean and standard deviation of the binned values, respectively.

fact that the $W_1 - W_2$ colour exhibits a tighter correlation with source redshift (Curran & Duchesne 2018) suggests that, due to the Malmquist bias, higher AGN activity is being detected at higher redshift, thus contributing to the determination of the photometric redshifts (Curran & Moss 2019). Therefore, the MIR magnitudes should also be useful in tracing rest-frame NIR (W_1 & W_2). However, this would not take effect until $z \gtrsim 5$.

3.3.2 Current limitations

In order to investigate the source of the inaccuracies in z_{phot} , we perform a 10-dimensional linear regression of the magnitudes and spectroscopic redshift versus Δz (Table 2). Although, most of the parameters are significant ($|t| \gtrsim 3\sigma$), as discussed above, the NIR (W_1) and UV (NUV) appear to be extremely important.

We also note the high significance of z_{spec} and, plotting this against Δz (Fig. 15), we see that the positive Δz values at $z_{\text{spec}} \gtrsim 2$ are more extreme than the negative ones at $z_{\text{spec}} \lesssim 1$. Referring to Fig. 13, at $z_{\text{spec}} \sim 2$ only the bluer rest-frame bands (FUV to u) are observed (over g to z), with no coverage until z in the rest-frame (W_1 observed). That is, the large gap between the observed z and W_1 bands, manifests in a loss of crucial data (g, r, i) in the rest-frame, leading to the drop in accuracy at $z_{\text{spec}} \gtrsim 2$.

This gap could potentially be covered with the inclusion of the 2MASS J, H, K bands (see Fig. 1), which were included in our

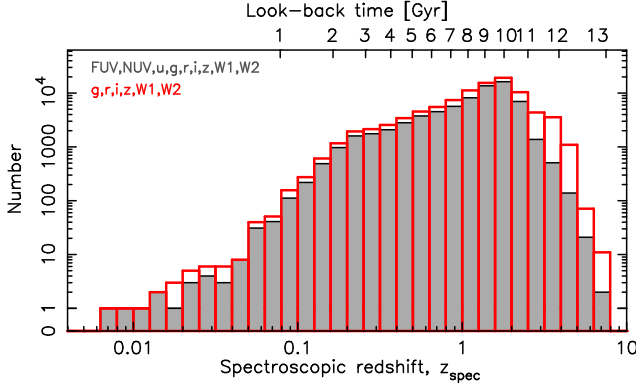


Figure 16. The redshift distribution for the SDSS QSOs with all nine magnitudes (filled – 71 267 sources) and those with $g, r, i, z, W1, W2$ magnitudes (unfilled – 95 351 sources). It is seen that the additional 23 084 sources mostly have redshifts $z \gtrsim 2$.

mining of the photometry (Sect. 2.1), cf. the UKIDSS Y, J, H, K bands included by Brescia et al. (2013), Sect. 3.1. However, the inclusion of these bands reduces the sample to just 19 077 QSOs. Using an 80:20 training:testing split, we obtain very similar results to our standard $u, g, r, i, z, W1, W2, NUV, FUV$ model, but with the validation sample reduced from 14 253 to 3815. Note that the implementation of a similarly wide array of bands has been used to yield photometric redshifts through template fitting, specifically by Ananna et al. (2017) who obtain $\sigma_{\text{NMAD}} = 0.06$ for 5961 X-ray sources in Stripe 82.

3.3.3 Excluding the blue and UV data

Given the disadvantage of requiring all nine magnitudes and the fact that the “bluer” bands (u, NUV, FUV) are more likely to be undetected, particularly at high redshift (Fig. 16), we investigate the effect of removing these magnitudes from the DL model. Excluding these gives a matching coincidence of 95%, cf. 71% of the original sample (Sect. 2.1). As before, we use an 80:20 training-validation split on the SDSS data, giving a validation sample of 19 070 QSOs with the $g, r, i, z, W1, W2$ magnitudes. From Fig. 17, we see a considerable spread in Δz ($\sigma_{\Delta z}[\text{data}] = 0.429$) compared to the full $FUV, NUV, u, g, r, i, z, W1, W2$ complement ($\sigma_{\Delta z}[\text{data}] = 0.235$). Since the UV magnitudes may be important in tracing the AGN activity at low redshift (Sect. 3.3.1), we expect that most of the uncertainty, due to the omission of the bluer magnitudes, would occur at $z \sim 0$. This is confirmed in Fig. 18, where the previous inaccuracy at $z \gtrsim 2$ appears also to be exacerbated (cf. Fig. 15). In summary, although the exclusion of the colours which use the u, NUV, FUV magnitudes does increase the number of high redshift detections, this is at the expense of the low redshift accuracy, with the additional high redshift estimates gained being of relatively low quality.

The multi-dimensional linear regression of the magnitudes versus Δz (Table 2) suggests that both the NUV and u magnitudes are especially crucial in obtaining a reliable photometric redshift. Examining the redshift distribution of the magnitudes (Fig. 19), we see that the NUV magnitude climbs rapidly at $z \gtrsim 1$ and the u at $z \gtrsim 2$, which is consistent with the rest-frame $\lambda = 1216 \text{ \AA}$ Lyman-break. The FUV magnitude also exhibits this at the expected $z \gtrsim 0.3$, although as established from Figs. 1, 6 & 7, this band is not expected to be reliable at $z \gtrsim 2$.

The poorer performance resulting from the exclusion of the

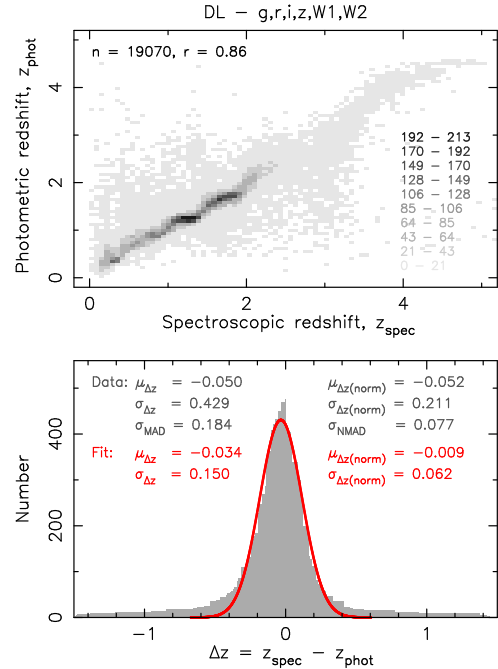


Figure 17. As Fig. 2 (right) – the predictions based on the DL method on the SDSS sample, but excluding the colours which use u and GALEX magnitudes.

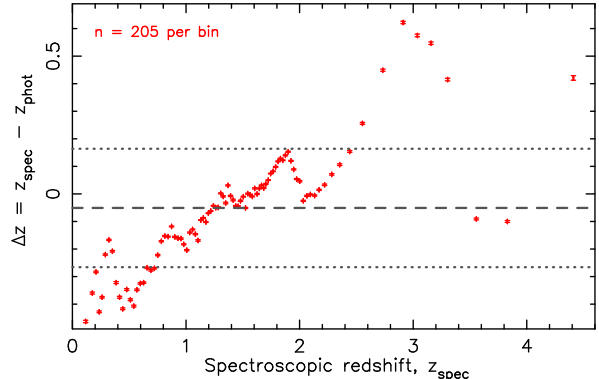


Figure 18. As Fig. 15, but excluding the “bluer” (u, NUV, FUV) magnitudes and binned into 93 bins of 205 QSOs each (leaving 5 remaining). The error bars show the standard error σ/\sqrt{n} and dashed and dotted lines show the mean and standard deviation of the binned values, respectively.

bluer magnitudes, suggests that the algorithm relies heavily upon the Lyman-break in estimating the redshift. The fact that both of these magnitudes peter out (at $NUV \gtrsim 22$ & $u \gtrsim 20$) is most likely responsible for the poor photometric redshifts estimates at high redshift. Improving upon this would require an automated and reliable method of including the non-detections or targeted longer integrations upon the sources of interest. Nevertheless, from Fig. 15, it appears that the photometric redshifts are statistically accurate up to $z \sim 2.5$, which, at a look-back time of 11 Gyr, covers the past 80% of cosmic history.

4 CONCLUSIONS

Forthcoming radio continuum surveys on the next generation of telescopes are expected to yield vast numbers of sources for which

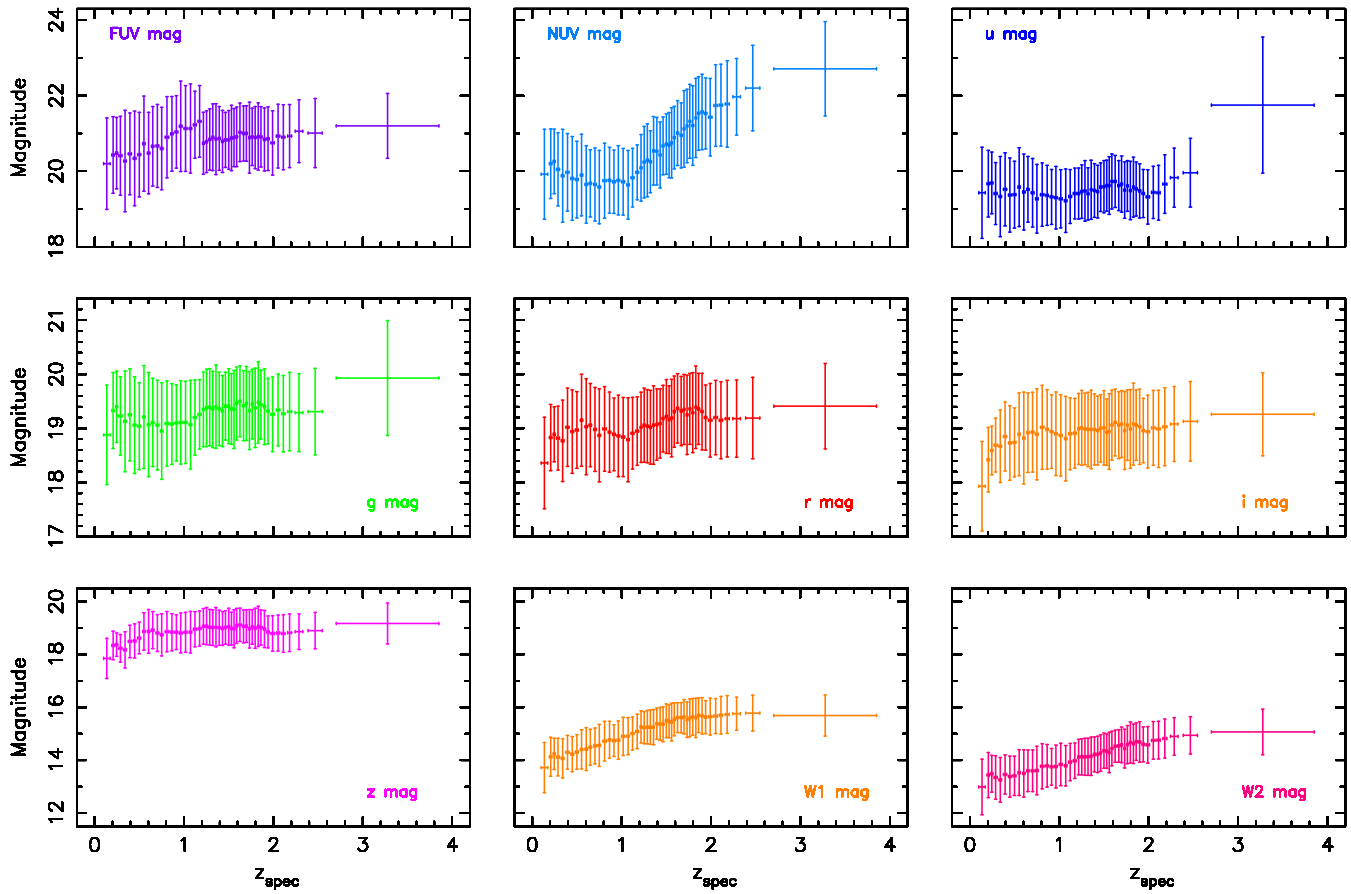


Figure 19. The magnitude versus redshift for the SDSS validation sample in 50 bins of 151 QSOs (leaving one remaining). As mentioned above, the high redshift *FUV* data are probably unreliable.

the redshifts will be unknown. Since these are observationally expensive to obtain, as well as introducing a bias towards the most optically bright objects, a rapid method of estimating accurate redshifts from the photometry would vastly increase the scientific value of these surveys.

Given the large datasets involved, machine learning is the most promising means. While there has been success training the algorithms on optical (SDSS) photometry alone, we have previously shown that the combination of SDSS, WISE *W1* & *W2* and GALEX colours leads to a significant increase in accuracy (Curran 2020). Here we compare our previous method, the *k*-Nearest Neighbour, with the Decision Tree Regression and Deep Learning methods. Mining the *FUV*, *NUV*, *u*, *g*, *r*, *i*, *z*, *W1*, *W2* photometry of the 100 000 QSOs selected from the SDSS DR12, gives 71 267 sources which are detected in all nine bands. Testing the full sample and various sub-samples shows the DL algorithm to perform the best, as measured by the (normalised) standard deviation, the (normalised) median absolute deviation, the regression coefficient and the gradient of the linear fit between the predicted and measured redshifts. Training the DL algorithm on 80% of the SDSS sample and validating on the other 20%, yields an accuracy of $\Delta z < 0.1$ up to $z \sim 2.5$ which corresponds to look-back times of 11 Gyr.

In order to determine the suitability of the DL model in predicting redshifts for other, radio-selected, samples, as for the SDSS sample, we scrape the photometry from various databases and bin these into the appropriate bands. We then use our full SDSS DR12

sample to train the model and validate this on the other catalogues. We find this cross-training to be successful, yielding photometric redshifts up to $z \sim 4$, with a standard deviation in Δz of $\sigma_{\Delta z}[\text{data}] \approx 0.25 - 0.37$. This is despite the mean radio flux densities of the samples differing by two orders of magnitude from the training sample, as well as there being a clear difference in the mean optical SEDs (cf. Elvis et al. 1994).

As per the KNN and other methods (Bovy et al. 2012; Brescia et al. 2013), the accuracy of the photometric redshift predictions depends heavily upon the addition of the infrared and ultra-violet photometry to the standard *u*, *g*, *r*, *i*, *z* (Richards et al. 2001; Weinstein et al. 2004; Ball et al. 2008; Maddox et al. 2012; Han et al. 2016). As noted by Curran & Moss (2019), over a large range of redshifts, a given rest-frame magnitude could occur in several other bands. This suggests that the mid-infrared *W3* & *W4* bands may be important at $z \gtrsim 5$, where the data are currently sparse, and that the current loss in accuracy at $z \gtrsim 2$ is due to the large gap between the SDSS and WISE bands. This could be somewhat remedied with the inclusion of the NIR *J*, *H*, *K* bands (Brescia et al. 2013), although the large reduction in sample size prevents this being the case for our sample.

Our data scraping and binning of the photometry has the advantage over other methods which use the SDSS magnitudes directly in that it produces a model that can be used to train other samples which may have little SDSS, but other optical photometry available (e.g. *B*, *G*, *V*, *R*). Our DL method has the advantage over similar applications of neural networks in that it utilises an

off-the-shelf deep learning library with basic hyperparameters – two *ReLU* layers and one *tanh* layer each comprising 200 neurons. It also runs rapidly on a standard laptop computer, compared to the DCMDN method (D’Isanto & Polsterer 2018), which requires a cluster, and the MLPQNA method (Brescia et al. 2013), which requires the prior “pruning” of features in order to speed up the computation. The main disadvantage, common to these other methods, is the requirement of the detection of the source over nine different observing bands, particularly the GALEX bands which are the most restrictive. Furthermore, the requirement of SDSS magnitudes to validate the all-sky surveys halves the number of sources which can be used. This highlights the need for southern sky training data (e.g. using SkyMapper), if the aim is to obtain photometric redshifts for continuum sources detected with the SKA.

ACKNOWLEDGEMENTS

We wish to thank the referee for their very helpful comments. This research has made use of the NASA/IPAC Extragalactic Database (NED) which is operated by the Jet Propulsion Laboratory, California Institute of Technology, under contract with the National Aeronautics and Space Administration and NASA’s Astrophysics Data System Bibliographic Service. This research has also made use of NASA’s Astrophysics Data System Bibliographic Service. Funding for the SDSS has been provided by the Alfred P. Sloan Foundation, the Participating Institutions, the National Science Foundation, the U.S. Department of Energy, the National Aeronautics and Space Administration, the Japanese Monbukagakusho, the Max Planck Society, and the Higher Education Funding Council for England. This publication makes use of data products from the Wide-field Infrared Survey Explorer, which is a joint project of the University of California, Los Angeles, and the Jet Propulsion Laboratory/California Institute of Technology, funded by the National Aeronautics and Space Administration. This publication makes use of data products from the Two Micron All Sky Survey, which is a joint project of the University of Massachusetts and the Infrared Processing and Analysis Center/California Institute of Technology, funded by the National Aeronautics and Space Administration and the National Science Foundation. GALEX is operated for NASA by the California Institute of Technology under NASA contract NAS5-98034.

DATA AVAILABILITY

Data and SDSS TensorFlow training model available on request.

REFERENCES

- Alam S. et al., 2015, *ApJS*, 219, 12
 Ananna T. T. et al., 2017, *ApJ*, 850, 66
 Ansari R. et al., 2019, *A&A*, 623, A76
 Assef R. J. et al., 2010, *ApJ*, 713, 970
 Ball N. M., Brunner R. J., Myers A. D., Strand N. E., Alberts S. L., Tcheng D., 2008, *ApJ*, 683, 12
 Barvainis R., 1987, *ApJ*, 320, 537
 Beck R., Szapudi I., Flewelling H., Holmberg C., Magnier E., 2021, *MNRAS*, 500, 1633
 Becker R. H., White R. L., Helfand D. J., 1995, *ApJ*, 450, 559
 Bianchi L., Shiao B., Thilker D., 2017, *ApJS*, 230, 24
 Bovy J. et al., 2012, *ApJ*, 749, 41
 Brescia M., Cavuoti S., D’Abrusco R., Longo G., Mercurio A., 2013, *ApJ*, 772, 140
 Brescia M., Cavuoti S., Longo G., De Stefano V., 2014, *A&A*, 568, A126
 Brookes M. H., Best P. N., Peacock J. A., Röttgering H. J. A., Dunlop J. S., 2008, *MNRAS*, 385, 1297
 Callingham J. R. et al., 2017, *ApJ*, 836, 174
 Ching J. H. Y. et al., 2017, *MNRAS*, 464, 1306
 Curran S. J., 2020, *MNRAS*, 493, L70
 Curran S. J., Duchesne S. W., 2018, *MNRAS*, 476, 3580
 Curran S. J., Hunstead R. W., Johnston H. M., Whiting M. T., Sadler E. M., Allison J. R., Athreya R., 2019, *MNRAS*, 484, 1182
 Curran S. J., Moss J. P., 2019, *A&A*, 629, A56
 Curran S. J. et al., 2011, *MNRAS*, 416, 2143
 Curran S. J., Whiting M. T., Murphy M. T., Webb J. K., Longmore S. N., Pihlström Y. M., Athreya R., Blake C., 2006, *MNRAS*, 371, 431
 D’Isanto A., Polsterer K. L., 2018, *A&A*, 609, 111
 Donoso E. et al., 2012, *ApJ*, 748, 80
 Drinkwater M. J. et al., 1997, *MNRAS*, 284, 85
 Duncan K. J. et al., 2018, *MNRAS*, 473, 2655
 Edelson R., Malkan M., 1986, *ApJ*, 308, 59
 Elvis M. et al., 1994, *ApJS*, 95, 1
 Han B., Ding H.-P., Zhang Y.-X., Zhao Y.-H., 2016, *Research in Astronomy and Astrophysics*, 16, 74
 Hickox R. C., Myers A. D., Greene J. E., Hainline K. N., Zakamska N. L., DiPompeo M. A., 2017, *ApJ*, 849, 53
 Ivezić Ž., Connolly A., VanderPlas J., Gray A., 2014, *Statistics, Data Mining, and Machine Learning in Astronomy: A Practical Python Guide for the Analysis of Survey Data*. Princeton University Press
 Jackson C. A., Wall J. V., Shaver P. A., Kellermann K. I., Hook I. M., Hawkins M. R. S., 2002, *A&A*, 386, 97
 Jarrett T. H. et al., 2011, *ApJ*, 735, 112
 Laurino O., D’Abrusco R., Longo G., Riccio G., 2011, *MNRAS*, 418, 2165
 Luken K. J., Norris R. P., Park L. A. F., 2019, *PASP*, 131, 108003
 Ma C. et al., 2009, *IERS Technical Note*, 35, 1
 Maddox N., Hewett P. C., Péroux C., Nestor D. B., Wisotzki L., 2012, *MNRAS*, 424, 2876
 Majic R. A. M., Curran S. J., 2015, *Radio Photometric Redshifts: Estimating radio source redshifts from their spectral energy distributions*. Tech. rep., Victoria University of Wellington
 Malkin Z., 2018, *ApJS*, 239, 20
 Morganti R., Sadler E. M., Curran S., 2015, *Advancing Astrophysics with the Square Kilometre Array (AASKA14)*, 134
 Norris R. P. et al., 2011, *PASA*, 28, 215
 Norris R. P. et al., 2019, *PASP*, 131, 108004
 Pâris I. et al., 2012, *A&A*, 548, A66
 Pâris I. et al., 2018, *A&A*, 613, A51
 Pasquet-Itam J., Pasquet J., 2018, *A&A*, 611, A97
 Reed S. L. et al., 2015, *MNRAS*, 454, 3952
 Richards G. T. et al., 2001, *AJ*, 122, 1151
 Salvato M., Ilbert O., Hoyle B., 2019, *Nature Astronomy*, 3, 212
 Schneider D. P. et al., 2010, *AJ*, 139, 2360
 Skrutskie M. F. et al., 2006, *AJ*, 131, 1163
 Tagliaferri R. et al., 2003, *Neural Networks*, 16, 297
 Weinstein M. A. et al., 2004, *ApJS*, 155, 243
 White R. L., Becker R. H., Helfand D. J., Gregg M. D., 1997, *ApJ*, 475, 479
 Wolf C. et al., 2018, *PASA*, 35, 10

Wright E. L. et al., 2010, AJ, 140, 1868
Yang Q. et al., 2017, AJ, 154, 269